Computational Mechanics manuscript No.
(will be inserted by the editor)

Building a Certified Reduced Basis for Coupled Thermo-Hydro-Mechanical Systems with Goal-Oriented Error Estimation

Ygee Larion · Sergio Zlotnik · Thierry J. Massart · Pedro Díez

Received: date / Accepted: date

Abstract A goal-oriented a-posteriori error estimator is developed for transient coupled Thermo - Hydro - Mechanical (THM) parametric problems solved with a reduced basis approximation. The estimator assesses the error in some specific Quantity of Interest (QoI). The goal-oriented error estimate is derived based on explicitly-computed weak residual of the primal problem and implicitly-computed adjoint solution associated with the QoI. The time-dependence of the coupled THM system poses an additional complexity as the auxiliary adjoint problem evolves backwards in time. The error estimator guides a greedy adaptive procedure that constructs progressively an optimal reduced basis by smartly selecting snapshot points over a given parametric training sample. The reduced basis obtained is used to drastically reduce the coupled system spatial degrees of freedom by several orders of magnitude. The computational gain obtained from the developed methodology is demonstrated through applications in 2D and 3D parametrized problems simulating the evolution of coupled THM processes in rock masses.

Y. Larion · T. J. Massart
Building, Architecture & Town Planning,
Structural and Material Computational Mechanics Group (BATIR-SMC), Université libre de Bruxelles
CP 194/2, Avenue F.D. Roosevelt 50, 1050 Brussels, Belgium
(✉larion.ygee@gmail.com, ✉thmassar@ulb.ac.be)

Y. Larion · S. Zlotnik · P. Díez
Laboratori de Càlcul Numèric, E.T.S. de Ingeniería de Caminos, Universitat Politècnica de Catalunya
Campus Nord UPC, 08034 Barcelona, Spain

S. Zlotnik · P. Díez
International Centre for Numerical Methods in Engineering (CIMNE) Barcelona, Spain

Keywords Model reduction · Reduced basis method · Goal-oriented error estimation · Adjoint problem · Coupled system · THM coupling

1 Introduction

Numerous studies have been conducted on coupled THM systems related to the behavior of geological formations for investigating the safety, performance and design optimization of underground nuclear waste repositories [1–7]. Over the years, some approaches started focusing on developing numerical models addressing these processes to support laboratory and in-situ tests validation [8–15]. These large-scale numerical models face the challenge of dealing with systems of high dimensionality related to large and complex geometrical discretizations, nonlinearity, a number of uncertain field parameters and prolonged time evolution. This issue becomes even more critical for certain types of problems requiring fast and multiple queries, for instance inverse identification problems. The standard finite element based solvers are computationally demanding and consequently, different high performance computing strategies are used to alleviate the computational burden [16–18].

Despite being widely used in many engineering fields for several years, there are very few studies that explored model order reduction applications to coupled geomechanical problems [19–21]. Model reduction techniques aim at reducing the dimensionality of a system by projecting the reference full order model to a low-dimensional subspace while preserving key information up to an acceptable level of accuracy. In the present contribution, we focus our attention on the reduced basis (RB) method - an enrichment-based class of model

order reduction that requires an adaptive strategy to construct a low-dimensional subspace spanning solutions of a system under parametric variation. Given a training sample that describes the parametric variation, it is desired to accurately approximate the reference solution at a much lower computational cost for any parameter inside the training set. The construction of this low-dimensional subspace mainly involves the assembly and post-processing of so-called 'snapshots' that refer to full order solutions evaluated at specific parameter values in the training sample.

An efficient a-posteriori error estimator is crucial to optimally select snapshots inside the parametric training sample. The efficiency of an error estimator is characterized by its rigor, sharpness and computational cost. Many of the error estimation techniques exploit the relationship between the residual and the error approximation of the system. This class of techniques is based on the post-processing of the residual, which can be done either explicitly by integration of residuals, or implicitly by solving local problems using residuals as source terms [22]. In recent years, several research efforts have been devoted to residual-based a-posteriori error estimators in the context of reduced basis applications for different types of PDE problems [23–28].

In this contribution, we develop a goal-oriented a-posteriori error estimator for time-dependent coupled THM systems which assesses the error in specific features of the solution, termed as 'Quantity of Interest' (QoI). The time-dependence of the coupled THM system poses an additional complexity as it involves the computation of the auxiliary adjoint problem evolving backwards in time. Various implementations of goal-oriented error estimation for time-dependent problems have been investigated in [29–36]. Similar to the methodology presented in [30–32], the error estimates for the coupled THM system are derived based on the explicitly-computed weak residual of the primal problem and on the implicitly-computed adjoint solution associated with the QoI. The error estimates are fed to the greedy-based adaptive strategy to optimally select the snapshots and certify the RB-projected solutions. For computational efficiency, the implicitly-computed adjoint is evaluated only once and reused to obtain the error estimates for the entire parametric training sample.

The rest of the paper is organized as follows. In Section 2, we describe the model problem governing equations and present the notations for the discretized coupled THM system in full order and in reduced order form. In Section 3, a greedy adaptive strategy is proposed to optimally select the snapshot set used in the construction of the low-dimensional RB subspace. We derive the formulation of the backward-in-time evolving dual problem corresponding to the coupled THM system and develop the goal-oriented error estimation scheme in Section 4. Finally in Section 5, numerical examples for a regional model of glacier advance in 2D and 3D are presented in order to demonstrate the accuracy of the optimally built RB-approximation and the computational gain achieved with the proposed methodology.

2 Problem Statement

2.1 Governing Equations and Discretization of THM Coupled Systems

The coupled system for a fully-saturated porous geomaterial includes the three equations describing the deformation of the linearly-elastic body, the flow of the fluid phase and the heat conduction. The mechanical behavior is governed by poroelastic constitutive equations, while the hydraulic and thermal responses are governed by Darcy's law and Fourier's law, respectively. The classical conservation laws together with the constitutive relationships yield the governing equations for the time-dependent coupled THM system [37], resulting in an initial boundary value problem that reads: find temperature $T(\boldsymbol{x},t)$, displacement $\mathbf{u}(\boldsymbol{x},t)$ and pressure $p(\boldsymbol{x},t)$ with $\boldsymbol{x}\in\bar{\Omega}\subset\mathbb{R}^d$ and $t\in(0,t_f]$ such that

$$\begin{aligned} k_c\nabla^2 T-\rho c_p\dot{T}+Q&=0\\ G_D\nabla\cdot(\nabla\mathbf{u})+(G_D+\lambda)\nabla(\nabla\cdot\mathbf{u})&\\ -\alpha\nabla p-3K_D\alpha_s\nabla T&=0\\ -\frac{k}{\mu_f}\nabla\cdot(\nabla p)+\alpha\nabla\cdot\dot{\mathbf{u}}+\frac{1}{M}\dot{p}&\\ -[\phi 3\alpha_f+(\alpha-\phi)3\alpha_s]\dot{T}&=0 \end{aligned}\qquad \text{in } \Omega\times(0,t_f] \tag{1}$$

with Neumann boundary conditions,

$$\begin{aligned} -k_c\nabla_{\mathrm{n}}T&=g_{\mathrm{N}}\\ \boldsymbol{\sigma}_{ij}\mathbf{n}_j&=\boldsymbol{\tau}_{\mathrm{N}_i}\\ \frac{k}{\mu_f}\nabla_{\mathrm{n}}p&=\upsilon_{\mathrm{N}} \end{aligned}\qquad \text{on } \partial\Gamma_N\times(0,t_f] \tag{2}$$

Dirichlet boundary conditions,

$$\begin{aligned} T&=T_D\\ \mathbf{u}&=\mathbf{u}_D\\ p&=p_D \end{aligned}\qquad \text{on } \partial\Gamma_D\times(0,t_f] \tag{3}$$

and initial conditions

$$\begin{aligned} T&=T_0\\ \mathbf{u}&=\mathbf{u}_0\\ p&=p_0 \end{aligned}\qquad \text{in } \Omega\times\{t=0\} \tag{4}$$

where the notation of physical parameters in the system of equations are listed in Table 1.

We approximate the solution to the problem in (1) -(4) by the standard finite element (FE) method. The system is spatially discretized by associating the approximation to a mesh of characteristic size H in the functional space $\mathcal{Z}^H \subset \mathcal{H}_0^1(\Omega)$, $\mathcal{W}^H \subset \mathcal{H}_0^1(\Omega)$, $\mathcal{Q}^H \subset \mathcal{H}_0^1(\Omega)$:

$$\begin{aligned} T(\boldsymbol{x},t) &\approx T^H(\boldsymbol{x},t) = \sum_{i=1}^{\mathtt{n_{nodes}}} T_i(t)N_i(\boldsymbol{x}) = \mathbf{N}^\mathsf{T}\boldsymbol{T} \\ \mathbf{u}(\boldsymbol{x},t) &\approx \mathbf{u}^H(\boldsymbol{x},t) = \sum_{i=1}^{\mathtt{n_{nodes}}} \mathbf{u}_i(t)N_i(\boldsymbol{x}) = \tilde{\mathbf{N}}^\mathsf{T}\boldsymbol{U} \\ p(\boldsymbol{x},t) &\approx p^H(\boldsymbol{x},t) = \sum_{i=1}^{\mathtt{n_{nodes}}} p_i(t)N_i(\boldsymbol{x}) = \mathbf{N}^\mathsf{T}\boldsymbol{p} \end{aligned} \tag{5}$$

where $\boldsymbol{U} \in \mathbb{R}^{d\times \mathtt{n_{nodes}}}$, $\mathtt{n_{nodes}}$ is the number of nodes discretizing the field in Ω, while $\mathbf{N}$ and $\tilde{\mathbf{N}}$ are compact support shape functions. In the case of a 2D domain, $\mathbf{N}$ and $\tilde{\mathbf{N}}$ are expressed as $\mathbf{N} := [N_1(\boldsymbol{x})\ N_2(\boldsymbol{x})\ ...N_{\mathtt{n_{nodes}}}(\boldsymbol{x})]^\mathsf{T}$ and $\tilde{\mathbf{N}} :=$

$$\begin{bmatrix} N_1(\boldsymbol{x}) & 0 & N_2(\boldsymbol{x}) & 0 & ... & N_{\mathtt{n_{nodes}}}(\boldsymbol{x}) & 0 \\ 0 & N_1(\boldsymbol{x}) & 0 & N_2(\boldsymbol{x}) & ... & 0 & N_{\mathtt{n_{nodes}}}(\boldsymbol{x}) \end{bmatrix}.$$

For further use, we write the weak form of the problem (1) -(4) in a compact form as

$$\begin{aligned} B(T,\mathbf{u},p;z,\mathbf{w},q) &= L(z,\mathbf{w},q) \\ &\forall z \in \mathcal{Z}^H, \mathbf{w} \in \mathcal{W}^H, q \in \mathcal{Q}^H \end{aligned} \tag{6}$$

Table 1 Notation of physical parameters of the coupled THM system

Parameters	
K_D	bulk modulus of drained rock
G_D	shear modulus of the drained rock
α	Biot-Willis coefficient
M	constrained specific storage coefficient
μ_f	viscosity
k	permeability
ϕ	porosity
α_s	thermal expansion coefficient in the solid phase
α_f	thermal expansion coefficient in the fluid phase
c_p	specific heat
k_c	thermal conductivity
Q	heat source
ρ	solid density
ρ_f	fluid density
$\boldsymbol{\sigma}$	traction

where

$$\begin{aligned} B(T,\mathbf{u},p;z,\mathbf{w},q) = &\int_\Omega \frac{\partial z}{\partial x_j} k_c \frac{\partial T}{\partial x_j} d\Omega + \int_\Omega z\rho c_p \frac{\partial T}{\partial t} d\Omega \\ &+ \int_\Omega \frac{\partial \mathbf{w}}{\partial x_j} G \frac{\partial \mathbf{u}_i}{\partial x_j} d\Omega \\ &+ \int_\Omega \frac{\partial \mathbf{w}}{\partial x_i} (G+\lambda) \frac{\partial \mathbf{u}_j}{\partial x_j} d\Omega \\ &- \int_\Omega \mathbf{w}\alpha \frac{\partial p}{\partial x_i} d\Omega \\ &- 3\int_\Omega \mathbf{w} K_D \alpha_s \frac{\partial T}{\partial x_i} d\Omega \\ &- \int_\Omega \frac{\partial q}{\partial x_j} \frac{k}{\mu_f} \frac{\partial p}{\partial x_j} d\Omega \\ &+ \int_\Omega q \frac{1}{M} \frac{\partial p}{\partial t} d\Omega \\ &+ \int_\Omega q\alpha \frac{\partial}{\partial t} (\frac{\partial u_i}{\partial x_i}) d\Omega \\ &- \int_\Omega q[\phi 3\alpha_f + (\alpha-\phi)3\alpha_s] \frac{\partial T}{\partial t} d\Omega \end{aligned} \tag{7}$$

for $i,j = 1,2,3$ and

$$L(z,\mathbf{w},q) = \int_\Gamma z g_\mathrm{N} d\Gamma_N + \int_\Gamma \mathbf{w}\boldsymbol{\tau}_{\mathrm{N}_i} d\Gamma_N - \int_\Gamma q\upsilon_\mathrm{N} d\Gamma_N. \tag{8}$$

The substitution of the approximation (5) in the weak form (6) leads to the discrete matrix form,

$$\mathbb{K}\,\mathbb{U} + \mathbb{C}\,\dot{\mathbb{U}} = \mathbb{F} \tag{9}$$

$$\underbrace{\begin{bmatrix} \mathbf{K_H} & 0 & 0 \\ \mathbf{K_T} & \mathbf{K_U} & \mathbf{C_P} \\ 0 & 0 & \mathbf{K_P} \end{bmatrix}}_{\mathbb{K}} \underbrace{\begin{bmatrix} \boldsymbol{T} \\ \boldsymbol{U} \\ \boldsymbol{p} \end{bmatrix}}_{\mathbb{U}} + \underbrace{\begin{bmatrix} \mathbf{C_H} & 0 & 0 \\ 0 & 0 & 0 \\ \mathbf{C_T} & \mathbf{C_P^\mathsf{T}} & \mathbf{C_M} \end{bmatrix}}_{\mathbb{C}} \underbrace{\begin{bmatrix} \dot{\boldsymbol{T}} \\ \dot{\boldsymbol{U}} \\ \dot{\boldsymbol{p}} \end{bmatrix}}_{\dot{\mathbb{U}}} = \underbrace{\begin{bmatrix} \mathbf{F_T} \\ \mathbf{F_u} \\ \mathbf{F_p} \end{bmatrix}}_{\mathbb{F}} \tag{10}$$

where $\mathbb{K}$ contains the stiffness and conductivity matrices, $\mathbb{C}$ contains the capacity (time-dependent) matrices and $\mathbb{F}$ contains the corresponding vectors to $L(\cdot)$.

For the time discretization, a time-discrete framework in the interval $I \equiv (0, t_f]$ is considered such that the subintervals are denoted as $\{0 = t^0 < t^1 < ... < t^l < .... < t^\mathcal{L} = t_f\}$ for $l = 1,2,...,\mathcal{L}$. For notation purposes, let Δt^l be the characteristic time step of the time-discrete framework, measured as $\Delta t^l = t^l - t^{l-1}$. To perform the time integration, an Euler-Backward scheme is used and the space-time discrete problem is written as

$$\begin{aligned} \Delta t^l \mathbb{K}\mathbb{U}^{\,l} + \mathbb{C}\,\mathbb{U}^{\,l} &= \mathbb{C}\,\mathbb{U}^{\,l-1} + \Delta t^l \mathbb{F}^{\,l} \\ &\forall l \in 1,2,...,\mathcal{L} \end{aligned} \tag{11}$$

Due to a lack of inf-sup condition, the coupled THM system can show oscillating solution patterns when temperature, displacement and pore pressure are approximated by the same set of basis functions [38–40]. We therefore use Taylor-Hood finite element spaces, assigning quadratic basis functions for displacement and linear basis functions for pore pressure and temperature, to avoid instability in the coupled THM system [37, 41, 42].

2.2 Reduced Order Model (ROM)

Considering the physical parameter constants of the coupled THM system appearing in (1), we assume that the material properties depend on a set of parameter $\boldsymbol{\mu} = (\mu_1, ..., \mu_{\mathtt{n_{par.}}}) \in \mathcal{P} \subset \mathbb{R}^P$, $\mathtt{n_{par.}} \geq 1$. The system unknowns are then denoted with an additional dependency on a set of material parameter $(T(\boldsymbol{x}, t, \boldsymbol{\mu}), \mathbf{u}(\boldsymbol{x}, t, \boldsymbol{\mu}), p(\boldsymbol{x}, t, \boldsymbol{\mu}))$. Note that in the next part, we simplify the field notations by writing them as $(T(\boldsymbol{\mu}), \mathbf{u}(\boldsymbol{\mu}), p(\boldsymbol{\mu}))$ instead of the full form. The problem in the parametric form is expressed as follows: find $(T(\boldsymbol{\mu}), \mathbf{u}(\boldsymbol{\mu}), p(\boldsymbol{\mu})) \in \mathcal{Z}^H \times \mathcal{W}^H \times \mathcal{Q}^H$ such that

$$B(T(\boldsymbol{\mu}), \mathbf{u}(\boldsymbol{\mu}), p(\boldsymbol{\mu}); z, \mathbf{w}, q) = L(z, \mathbf{w}, q) \tag{12}$$

where

$$\begin{aligned} B(\cdot\,;\cdot) = &\int_\Omega \frac{\partial z}{\partial x_j} k_c(\boldsymbol{\mu}) \frac{\partial T}{\partial x_j} d\Omega + \int_\Omega z \rho c_p(\boldsymbol{\mu}) \frac{\partial T}{\partial t} d\Omega \\ &+ \int_\Omega \frac{\partial \mathbf{w}}{\partial x_j} G(\boldsymbol{\mu}) \frac{\partial \mathbf{u}_i}{\partial x_j} d\Omega + \int_\Omega \frac{\partial \mathbf{w}}{\partial x_i} (G(\boldsymbol{\mu}) \\ &+ \lambda(\boldsymbol{\mu})) \frac{\partial \mathbf{u}_j}{\partial x_j} d\Omega - \int_\Omega \mathbf{w} \alpha(\boldsymbol{\mu}) \frac{\partial p}{\partial x_i} d\Omega \\ &- 3 \int_\Omega \mathbf{w} K_D \alpha_s(\boldsymbol{\mu}) \frac{\partial T}{\partial x_i} d\Omega \\ &- \int_\Omega \frac{\partial q}{\partial x_j} \frac{k(\boldsymbol{\mu})}{\mu_(\boldsymbol{\mu}) f} \frac{\partial p}{\partial x_j} d\Omega \\ &+ \int_\Omega q \frac{1}{M(\boldsymbol{\mu})} \frac{\partial p}{\partial t} d\Omega \\ &+ \int_\Omega q \alpha(\boldsymbol{\mu}) \frac{\partial}{\partial t} (\frac{\partial \mathbf{u}_i}{\partial x_i}) d\Omega \\ &- \int_\Omega q [\phi(\boldsymbol{\mu}) 3 \alpha_f(\boldsymbol{\mu}) + (\alpha(\boldsymbol{\mu}) \\ &- \phi(\boldsymbol{\mu})) 3 \alpha_s(\boldsymbol{\mu})] \frac{\partial T}{\partial t} d\Omega \end{aligned} \tag{13}$$

for $i, j = 1, 2, 3$.

The approximate solution of the ROM is based on a standard Galerkin projection of the full order FE model to the global approximation spaces generated from well-chosen solutions (snapshots) evaluated at specific parameter and time values. Given a set of parameter values $\mathcal{M} = \{\boldsymbol{\mu}^1, ..., \boldsymbol{\mu}^N\}$, the snapshots contain the corresponding solutions $S^N = \{T(\boldsymbol{\mu}^1), \mathbf{u}(\boldsymbol{\mu}^1), p(\boldsymbol{\mu}^1), \ldots, T(\boldsymbol{\mu}^N), \mathbf{u}(\boldsymbol{\mu}^N), p(\boldsymbol{\mu}^N)\}$ where N is much smaller than the characteristic size of the reference full order model.

It is critical that the ROM inherits the crucial properties of the reference full order model − particularly, maintaining the numerical stability of the model to guarantee the accuracy and convergence of the ROM. There are numerous works dedicated to the stability of ROM, proposing strategies to develop stability preserving models for specific types of problem [44–47]. In general however, ensuring the numerical stability in model reduction is still an open issue. The numerical stability of the reduced coupled THM model is tackled similarly as in the FE context [38–40], by using different basis functions to approximate the displacement, pore pressure and temperature fields. Snapshot solutions are also orthonormalized to ensure algebraic stability for each basis.

We define the global approximation (RB) spaces separately for each of the field variable as follows:

$$\begin{aligned} \mathcal{Z}_N^H &= \text{span}\{T(\boldsymbol{\mu}^n), \quad 1 \leq n \leq \mathtt{n_{snapshots}}\} \quad \subset \mathcal{Z}^H \\ \mathcal{W}_N^H &= \text{span}\{\mathbf{u}(\boldsymbol{\mu}^n), \quad 1 \leq n \leq \mathtt{n_{snapshots}}\} \quad \subset \mathcal{W}^H \\ \mathcal{Q}_N^H &= \text{span}\{p(\boldsymbol{\mu}^n), \quad 1 \leq n \leq \mathtt{n_{snapshots}}\} \quad \subset \mathcal{Q}^H. \end{aligned} \tag{14}$$

To project the FE model to the set of RB spaces, the coupled system is 'decoupled' such that elements of the stiffness, conductivity and capacity matrices are extracted and grouped into blocks based on the field variable that it interacts with (15). Let $\mathbb{Z}, \mathbb{W}$ and $\mathbb{Q}$ denote the RB matrices for temperature, displacement and pressure, respectively. Each block is projected accordingly onto its corresponding basis, i.e., $\mathbf{K_T}$ interacts with temperature and displacement fields, therefore it is projected to the RB space from temperature ($\mathcal{Z}_N^H$) and displacement ($\mathcal{W}_N^H$) snapshots. Meanwhile, $\mathbf{K_P}$ that solely interacts with pore pressure is projected only to the RB space from pressure snapshots ($\mathcal{Q}_N^H$). These projected blocks are then reassembled in the same way as the FE coupled system as seen in (15) and (16), but the resulting blocks will have a much smaller characteristic size of order N.

$$\begin{aligned} &\begin{bmatrix} \mathbf{K_H}_N & 0 & 0 \\ \mathbf{K_T}_N & \mathbf{K_U}_N & \mathbf{C_P}_N \\ 0 & 0 & \mathbf{K_P}_N \end{bmatrix} \begin{bmatrix} \boldsymbol{T}_N \\ \boldsymbol{U}_N \\ \boldsymbol{p}_N \end{bmatrix} \\ &+ \begin{bmatrix} \mathbf{C_H}_N & 0 & 0 \\ 0 & 0 & 0 \\ \mathbf{C_T}_N & \mathbf{C}_{\mathbf{P}N}^{\mathsf{T}} & \mathbf{C_M}_N \end{bmatrix} \begin{bmatrix} \dot{\boldsymbol{T}}_N \\ \dot{\boldsymbol{U}}_N \\ \dot{\boldsymbol{p}}_N \end{bmatrix} = \begin{bmatrix} \mathbf{F_T}_N \\ \mathbf{F_u}_N \\ \mathbf{F_p}_N \end{bmatrix} \end{aligned} \tag{15}$$

$$
\begin{aligned}
\mathbf{K_H}_N &= \mathbb{Z}^\mathsf{T}\,\mathbf{K_H}\,\mathbb{Z} & \mathbf{K_T}_N &= \mathbb{W}^\mathsf{T}\,\mathbf{K_T}\,\mathbb{Z}\\
\mathbf{K_U}_N &= \mathbb{W}^\mathsf{T}\,\mathbf{K_U}\,\mathbb{W} & \mathbf{C_P}_N &= \mathbb{W}^\mathsf{T}\,\mathbf{C_P}\,\mathbb{Q}\\
\mathbf{K_P}_N &= \mathbb{Q}^\mathsf{T}\,\mathbf{K_P}\,\mathbb{Q} & \mathbf{C_H}_N &= \mathbb{Z}^\mathsf{T}\,\mathbf{C_H}\,\mathbb{Z}\\
\mathbf{C_T}_N &= \mathbb{Q}^\mathsf{T}\,\mathbf{C_T}\,\mathbb{Z} & \mathbf{C_P^\mathsf{T}}_N &= \mathbb{Q}^\mathsf{T}\,\mathbf{C_P}^T\,\mathbb{W}\\
\mathbf{C_M}_N &= \mathbb{Q}^\mathsf{T}\,\mathbf{C_M}\,\mathbb{Q} & \mathbf{F_T}_N &= \mathbb{Z}^\mathsf{T}\,\mathbf{F_T}\\
\mathbf{F_u}_N &= \mathbb{W}^\mathsf{T}\,\mathbf{F_u} & \mathbf{F_p}_N &= \mathbb{Q}^\mathsf{T}\,\mathbf{F_p}\\
\boldsymbol{T}_N &= \mathbb{Z}^\mathsf{T}\,\boldsymbol{T} & \boldsymbol{U}_N &= \mathbb{W}^\mathsf{T}\,\boldsymbol{U}\\
\boldsymbol{p}_N &= \mathbb{Q}^\mathsf{T}\,\boldsymbol{p}
\end{aligned}
\tag{16}
$$

Given $\boldsymbol{\mu} \in \mathcal{P}$, the approximated solutions belonging to the RB spaces ($T_N(\boldsymbol{\mu}) \in \mathcal{Z}_N^H$, $\mathbf{u}_N(\boldsymbol{\mu}) \in \mathcal{W}_N^H$, $p_N(\boldsymbol{\mu}) \in \mathcal{Q}_N^H$) are obtained by solving

$$
\begin{aligned}
&B(T_N(\boldsymbol{\mu}), \mathbf{u}_N(\boldsymbol{\mu}), p_N(\boldsymbol{\mu}); z, \mathbf{w}, q) = L(z, \mathbf{w}, q)\\
&\qquad \forall z \in \mathcal{Z}_N^H,\ \mathbf{w} \in \mathcal{W}_N^H,\ q \in \mathcal{Q}_N^H
\end{aligned}
\tag{17}
$$

where the dimensionality of the system corresponding to the left hand side $B(\,\cdot\,)$ and right hand side $L(\,\cdot\,)$ terms, as described in (15) and (16), is much lower than the full order FE model.

3 Generation of the Reduced Basis

The computational procedure involved in generating the reduced basis is explained in this section. The RB is built from an assembly of snapshot solutions of the full order model evaluated within a parametric training sample. Optimally selecting the parameters where such snapshots are evaluated is evidently critical for efficiently building the RB. It is desired that the selected snapshots give the most accurate approximation while keeping the number of snapshots to a minimum. In order to satisfy this requirement, we pursue an adaptive strategy in which the criterion to select the snapshots is driven by an a-posteriori error estimator. In turn, this error estimator also provides certification to the RB-approximated solution. The error estimator developed for the coupled THM system is discussed thoroughly in Section 4.

The adaptive strategy is implemented in a greedy-based sampling framework to build hierarchical RB approximation spaces [19, 24, 25, 43], in which the basis is enriched by appending new snapshot solutions at every enrichment step. The greedy adaptive strategy is explained by the schematic procedure below.

Given a parametric training sampling space discretization $\Xi_{train} \subset \mathtt{n_{sample}}$, with $\Xi_{train} = \text{span}\,\{\boldsymbol{\mu}^1,\ \boldsymbol{\mu}^2 \ldots,\ \boldsymbol{\mu}^{\mathtt{n_{sample}}}\}$, a stopping tolerance for estimated error ϵ, and a maximum number of enrichment steps N_{max}, initiate the greedy strategy at $N = 0$ with empty snapshot matrices $S_T^N, S_\mathbf{u}^N, S_p^N$ and a pre-selected initial parameter value $\boldsymbol{\mu}^* = \boldsymbol{\mu}^n$

while $N < N_{max}$ and $\delta_N > \epsilon$
  $N \leftarrow N + 1$
  $[T, \mathbf{u}, p] = \mathbf{FE}(\boldsymbol{\mu}^*)$
  $S_T^N = [S_T^{N-1}; T],\ S_\mathbf{u}^N = [S_\mathbf{u}^{N-1}; \mathbf{u}],\ S_p^N = [S_p^{N-1}; p]$
  $\mathbb{V}_T = \mathbf{POD}(S_T^N), \mathbb{V}_\mathbf{u} = \mathbf{POD}(S_\mathbf{u}^N), \mathbb{V}_p = \mathbf{POD}(S_p^N)$
  for $\boldsymbol{\mu} \in \Xi_{train}$
    $\Delta(\boldsymbol{\mu}) = \mathbf{ERROR\ ESTIMATE}(\mathbb{V}_T, \mathbb{V}_\mathbf{u}, \mathbb{V}_p, \boldsymbol{\mu})$
  end
  $\boldsymbol{\mu}^* = \arg \max_{\boldsymbol{\mu} \subset \Xi_{train}} \Delta(\boldsymbol{\mu})$
  $\delta_N = \max_{\boldsymbol{\mu} \subset \Xi_{train}} \Delta(\boldsymbol{\mu})$
end

In the first enrichment step, a full order space-time FE solution is evaluated at a pre-selected parameter value and denoted as a snapshot. To construct the basis for each field, the snapshot is separated ($S_T^N, S_\mathbf{u}^N, S_p^N$) and orthonormalized with the Proper Orthogonal Decomposition (POD) technique. The modes are truncated by prescribing a tolerance that corresponds to their energy contribution relative to the contribution of the first mode. The same tolerance level is prescribed for temperature, displacement and pore pressure fields, which results in a number of truncated modes that can vary accordingly, reflecting the different features of each snapshot field (see Figure 6).Using the truncated and orthonormalized matrices as projection bases, the error estimator selects the point in the training sample which gives the worst (least accurate) approximation in the current RB space. The next step is to generate snapshot solutions at this worst point and append it to the RB space to improve its approximation. The enrichment procedure is repeated until the stopping criteria are satisfied.

The most critical ingredient in the RB generation strategy is to ensure that the error estimator gives a good approximation of the exact error, while being computationally inexpensive. Particularly for cases where the training sample is very large, estimating the error at every set of parameter value is an exhaustive procedure.

4 Goal-Oriented Error Estimation

4.1 Error-Residual Representation

Residual-based a-posteriori error estimators are typically employed to certify reduced order models built

from projection-based techniques. In goal-oriented error estimation, we focus on specific features of the solution (QoI) and assess the error in these features. The error in the QoI is estimated by relating the primal residual to an appropriate adjoint solution of a dual problem [30,34–36]. The ideas introduced in [30–32], in which an implicitly-solved adjoint is directly injected into the weak primal residual of a parabolic PDE, are followed to develop an a-posteriori goal-oriented error estimator for the coupled THM system.

We represent the error in the the temperature, displacement and pore pressure fields between the reference FE and RB-projected solution as

$$e = (e_T, e_{\mathbf{u}}, e_p) = (T - T_N, \mathbf{u} - \mathbf{u}_N, p - p_N). \tag{18}$$

Recalling the weak form of the model problem (6) we define the residual as

$$\begin{aligned} R(z, \mathbf{w}, q) &= B(e_T, e_{\mathbf{u}}, e_p; z, \mathbf{w}, q) \\ &= L(z, \mathbf{w}, q) - B(T_N, \mathbf{u}_N, p_N; z, \mathbf{w}, q) \\ &\qquad \forall z \in \mathcal{Z}^H, \mathbf{w} \in \mathcal{W}^H, q \in \mathcal{Q}^H. \end{aligned} \tag{19}$$

Denoting the QoI as $J(\cdot)$, we introduce a corresponding dual problem. Let $T_{adj} \in \mathcal{Z}^H$, $\mathbf{u}_{adj} \in \mathcal{W}^H$, $p_{adj} \in \mathcal{Q}^H$ be the set of adjoint solutions to the dual problem such that

$$B(\,\cdot\,; T_{adj}, \mathbf{u}_{adj}, p_{adj}) = J(\,\cdot\,). \tag{20}$$

It is aimed to evaluate the QoI, $J(T, \mathbf{u}, p)$, without having to explicitly compute the primal solution $(T, \mathbf{u}, p)$. The QoI is estimated by relating the source term of the primal problem to the adjoint solution of the dual problem.

$$J(T, \mathbf{u}, p) = L(T_{adj}, \mathbf{u}_{adj}, p_{adj}) \tag{21}$$

and consequently, we can write the error in the QoI as an adjoint-residual representation

$$\begin{aligned} J(e_T, e_{\mathbf{u}}, e_p) &= R(T_{adj}, \mathbf{u}_{adj}, p_{adj}) \\ &= L(T_{adj}, \mathbf{u}_{adj}, p_{adj}) \\ &\quad - B(T_N, \mathbf{u}_N, p_N; T_{adj}, \mathbf{u}_{adj}, p_{adj}). \end{aligned} \tag{22}$$

The implementation of adjoint-residual error representation is simple once the adjoint solution and weak residuals are computed − the adjoint solution is directly plugged in to the residual at every time step, adapting the space-time grid. Particularly for weak residuals $R(\cdot)$ which are explicitly evaluated, the computational cost is minimal even if solved for each parameter value in the training sample. In contrast, computing the backward-in-time-evolving adjoint solution of the dual problem is more involved and computationally expensive.

4.2 Backward-in-Time Evolving Adjoint Solution of a Dual Problem

For the QoI, we consider a general functional output that accounts for the behavior of the solution evolving over time

$$\begin{aligned} J(T, \mathbf{u}, p) = &\int_0^{t_f} \int_\Omega \bar{f}_T(\boldsymbol{x}, t) T \; d\Omega \; dt \\ &+ \int_0^{t_f} \int_\Omega \bar{\mathbf{f}}_{\mathbf{u}}(\boldsymbol{x}, t) \mathbf{u} \; d\Omega \; dt \\ &+ \int_0^{t_f} \int_\Omega \bar{f}_p(\boldsymbol{x}, t) p \; d\Omega \; dt \end{aligned} \tag{23}$$

For the sake of simplicity, we normalize the terms to have consistent units with contributions from the temperature, displacement and pore pressure fields resulting to a scalar QoI bearing the unit of the chosen field. By choosing the QoI to have the unit of displacement field, we introduce the following characteristic factors derived from norms of a previously solved primal problem

$$\hat{\gamma} = \|\mathbf{u}\| / \|T\|; \qquad \hat{T} = \hat{\gamma} T \tag{24}$$

$$\hat{\delta} = \|\bar{\mathbf{f}}_{\mathbf{u}}\| / \|\bar{f}_T\|; \quad \hat{f_T} = \hat{\delta} \bar{f}_T \tag{25}$$

$$\hat{\alpha} = \|\mathbf{u}\| / \|p\|; \qquad \hat{p} = \hat{\alpha} p \tag{26}$$

$$\hat{\beta} = \|\bar{\mathbf{f}}_{\mathbf{u}}\| / \|\bar{f}_p\|; \quad \hat{f}_p = \hat{\beta} \bar{f}_p. \tag{27}$$

Making use of the arbitrary characteristic factors, the QoI in (23) is expressed as

$$\begin{aligned} \hat{J}(T, \mathbf{u}, p) = \hat{\gamma} &\int_0^{t_f} \int_\Omega \bar{f}_T(\boldsymbol{x}, t) T \; d\Omega \; dt \\ &+ \int_0^{t_f} \int_\Omega \bar{\mathbf{f}}_{\mathbf{u}}(\boldsymbol{x}, t) \mathbf{u} \; d\Omega \; dt \\ &+ \hat{\alpha} \int_0^{t_f} \int_\Omega \bar{f}_p(\boldsymbol{x}, t) p \; d\Omega \; dt. \end{aligned} \tag{28}$$

Recalling the dual problem associated with the coupled THM system,

$$\begin{aligned} B(z, \mathbf{w}, q; T_{adj}, \mathbf{u}_{adj}, p_{adj}) &= J(z, \mathbf{w}, q) \\ \forall z \in \mathcal{Z}^H, \mathbf{w} \in \mathcal{W}^H, q \in \mathcal{Q}^H & \end{aligned} \tag{29}$$

it is observed that due to the coupling terms in the system of equations, the ensemble of units in the left hand side $B(\,\cdot\,)$ is only compatible with the right hand side of the primal problem $L(\,\cdot\,)$, and not with $J(z, \mathbf{w}, q)$. It becomes critical to express the left hand side of the dual problem (29) with normalized units in order to satisfy compatibility with the right hand side vector of the QoI. The dual problem bearing compatible units is therefore written as:

$$\hat{B}(z, \mathbf{w}, q; T_{adj}, \mathbf{u}_{adj}, p_{adj}) = J(z, \mathbf{w}, q) \tag{30}$$

where

$$\begin{aligned}
\hat{B}(\cdot\,;\cdot) = &\frac{\hat{\delta}}{\hat{\gamma}} \int_0^T \int_\Omega \frac{\partial T_{adj}}{\partial x} k_c \frac{\partial z}{\partial x} d\Omega dt \\
&+ \int_0^T \int_\Omega \frac{\partial \mathbf{u}_{adj}}{\partial x} G \frac{\partial \mathbf{w}}{\partial x} d\Omega dt \\
&+ \int_0^T \int_\Omega \frac{\partial \mathbf{u}_{adj}}{\partial x} (G+\lambda) \frac{\partial \mathbf{w}}{\partial x} d\Omega dt \\
&- \frac{1}{\hat{\alpha}} \int_0^T \int_\Omega \frac{\partial p_{adj}}{\partial x} \alpha \mathbf{w} d\Omega dt \\
&- \frac{1}{\hat{\gamma}} \int_0^T \int_\Omega T_{adj}\, 3K_D \alpha_s \frac{\partial \mathbf{w}}{\partial x} d\Omega dt \\
&- \frac{\hat{\beta}}{\hat{\alpha}} \int_0^T \int_\Omega \frac{\partial p_{adj}}{\partial x} \kappa \frac{\partial q}{\partial x} d\Omega dt \\
&+ \frac{\hat{\delta}}{\hat{\gamma}} \int_\Omega T_{adj}(t=T) \rho c_p z d\Omega \\
&- \frac{\hat{\delta}}{\hat{\gamma}} \int_0^T \int_\Omega z \rho c_p \frac{\partial T_{adj}}{\partial t} d\Omega dt \\
&+ \frac{\hat{\beta}}{\hat{\alpha}} \int_\Omega p_{adj}(t=T) \frac{1}{M} q d\Omega \\
&- \frac{\hat{\beta}}{\hat{\alpha}} \int_0^T \int_\Omega q \frac{1}{M} \frac{\partial p_{adj}}{\partial t} d\Omega dt \\
&+ \hat{\beta} \int_\Omega \mathbf{u}_{adj}(t=T) \alpha \frac{\partial q}{\partial x} d\Omega \\
&- \hat{\beta} \int_0^T \int_\Omega \frac{\partial q}{\partial x} \alpha \frac{\partial \mathbf{u}_{adj}}{\partial t} d\Omega dt \\
&+ \frac{\hat{\beta}}{\hat{\gamma}} \int_\Omega T_{adj}(t=T)[\phi 3\alpha_f + (\alpha-\phi)3\alpha_s] q d\Omega \\
&- \frac{\hat{\beta}}{\hat{\gamma}} \int_0^T \int_\Omega q[\phi 3\alpha_f + (\alpha-\phi)3\alpha_s] \frac{\partial T_{adj}}{\partial t} d\Omega dt.
\end{aligned} \tag{31}$$

In strong compact form, the dual problem is thus written as:

$$\begin{aligned}
\frac{\hat{\delta}}{\hat{\gamma}} k_c \nabla^2 T_{adj} + \frac{\hat{\delta}}{\hat{\gamma}} \rho c_p \dot{T}_{adj} &= \bar{f}_T \\
G_D \nabla \cdot (\nabla \mathbf{u}_{adj}) + (G_D + \lambda) \nabla (\nabla \cdot \mathbf{u}_{adj}) & \\
- \frac{1}{\hat{\alpha}} \alpha \nabla p_{adj} - \frac{1}{\hat{\gamma}} 3K_D \alpha_s \nabla T_{adj} &= \bar{\mathbf{f}}_{\mathbf{u}} \\
- \frac{\hat{\beta}}{\hat{\alpha}} \frac{k}{\mu_f} \nabla \cdot (\nabla p_{adj}) - \hat{\beta} \alpha \nabla \cdot \dot{\mathbf{u}}_{adj} & \\
- \frac{\hat{\beta}}{\hat{\alpha}} \frac{1}{M} \dot{p}_{adj} + \frac{\hat{\beta}}{\hat{\gamma}} [\phi 3\alpha_f + (\alpha-\phi)3\alpha_s] \dot{T}_{adj} &= \bar{f}_p \\
\text{in } \Omega \times (0, t_f]&
\end{aligned} \tag{32}$$

with Neumann boundary conditions,

$$\begin{aligned}
-k_c \nabla_{\mathrm{n}} T_{adj} &= 0 \\
\boldsymbol{\sigma}_{ij,adj} \mathbf{n}_j &= \mathbf{0} \\
\frac{k}{\mu_f} \nabla_{\mathrm{n}} p_{adj} &= 0
\end{aligned} \qquad \text{on } \partial\Gamma_N \times (0, t_f] \tag{33}$$

Dirichlet boundary conditions,

$$\begin{aligned}
T_{adj} &= 0 \\
\mathbf{u}_{adj} &= 0 \\
p_{adj} &= 0
\end{aligned} \qquad \text{on } \partial\Gamma_D \times (0, t_f] \tag{34}$$

and initial conditions

$$\begin{aligned}
T_{adj} &= 0 \\
\mathbf{u}_{adj} &= 0 \\
p_{adj} &= 0
\end{aligned} \qquad \text{in } \Omega \times \{t = t^f\}. \tag{35}$$

Note that the adjoint solution of each field $(T_{adj}, \mathbf{u}_{adj}, p_{adj})$ bears the same units arising from the characteristic factors $(\hat{\gamma}, \hat{\delta}, \hat{\alpha}, \hat{\beta})$ introduced in the coupled system of equations. This allows for the adjoint to be injected into the residual in a straightforward procedure that yields the error estimate in the QoI,

$$\hat{J}(e_T, e_{\mathbf{u}}, e_p) = \hat{R}(T_{adj}, \mathbf{u}_{adj}, p_{adj}) \tag{36}$$

where $\hat{R}$ contains the residuals from the temperature, displacement and pore pressure fields normalized to have consistent units.

The strong form of the dual problem is very similar to the primal problem differing only by the time-dependent terms that have opposite signs − reflecting the backward in time propagation of the adjoint solution. Evidently, the computational cost of solving the dual problem is the same as solving the primal problem.

In this methodology, note that only one adjoint solution is needed to represent the entire parametric training sample. Further details on this assumption will be explained in section 5.1.4.

5 Numerical Examples

5.1 2D Advancing Glacier Problem

As a first illustrative application, we consider a homogeneous region for a fully-saturated rock mass in a 2D domain, see Figure 1. A 22000m by 1700m rock mass is subjected to a glacier with non-uniform thickness advancing along the upper surface Γ_{TOP}. The thickness

variation of the glacier is described by the function $H(x,t)$ as inspired by reference [48],

$$H(x,t) = 2^{1/8} H_{max} \left(\frac{L - X + v\,t}{L} \right)^{1/2}. \tag{37}$$

where $H_{max} = 3200m$ is the maximum height of the glacier, $L = 1329870m$ is the distance from the center to the glacier front, X is the distance from the center of the glacier (the datum point) which is related to the coordinate system of the model domain by $X = x + 1333029m$, v is velocity of the glacier specified as 1.27 m per year. At $t = 0$, the glacier thickness function $H(X)$ satisfies $H(0) = H_{max}$ and $H(L) = 0$. For an observation period of 6000 years, the glacier thus moves 7620m on top of the upper surface Γ_{TOP} of the rock mass. The loading effects of glacier are treated as boundary conditions for the governing equations of the system. These effects are applied as traction ($\boldsymbol{\sigma}_N$) in the mechanical system, and as prescribed pore pressure (p_D) and temperature (T_D) on the upper surface. Additional Neumann and Dirichlet boundary conditions are imposed on the lower surface and edges of the rock mass, leading to

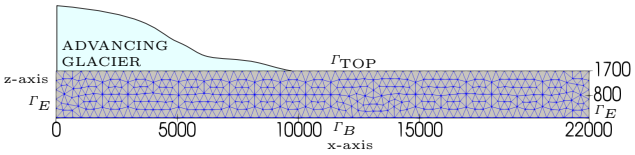

Fig. 1 Homogeneous rock mass subjected to glacier loading

$$\begin{aligned} \boldsymbol{\sigma}_{zz}(x,t) &= \boldsymbol{\sigma}_N = -\rho_f g H(x,t) \\ T(x,t) &= T_D = T_{\max} \frac{H(x,t)}{H_{\max}} \quad \text{on} \quad \partial\Gamma_{\text{TOP}} \\ p(x.t) &= p_D = \rho_f g H(x,t) \end{aligned} \tag{38}$$

$$\mathbf{u}_z = 0; \quad \frac{\partial p}{\partial z} = 0; \quad \frac{\partial T}{\partial z} = 0 \qquad \text{on} \quad \partial\Gamma_B \tag{39}$$

$$\mathbf{u}_n = 0; \quad \frac{\partial p}{\partial n} = 0; \quad \frac{\partial T}{\partial n} = 0 \qquad \text{on} \quad \partial\Gamma_E. \tag{40}$$

In this illustrative application, only changes in the rock mass response due to small glacier advances are investigated. Furthermore, the problem is assumed to be linear and that the initial fields at the onset of advancing glacier (i.e. stresses due to the weight of the glacier at its initial position, geostatic stresses, hydrostatic fluid pressure, temperature distribution from geothermal heat flux, etc.) can be ignored. Zero initial conditions are therefore imposed on the system.

Table 2 Physical parameters describing the homogeneous rock mass

K_D	2×10^{10} Pa
G_D	1.2×10^{10} Pa
α	0.70
M	3.08×10^{10} Pa
μ_f	1×10^{-3} Pa·s
k	1.55×10^{-19} m^2
ϕ	0.05
α_s	8.3×10^{-6} °C^{-1}
α_f	6.9×10^{-7} °C^{-1}
c_p	1.83×10^{6} N m^2 · K
k_c	3.66 W/ m · K

5.1.1 Primal Problem

The FE solution to the coupled THM problem (1-4) subjected to the glacier loading with the physical properties described in Table 2 is obtained from solving the discrete problem in (11). For spatial discretization, Taylor-Hood $P_2 - P_1$ elements on triangles are used - quadratic interpolation for displacements and linear interpolation for pore pressure and temperature. There are 4398 degrees of freedom (DOF) in total and the time grid is spaced by 100 logarithmically increasing timesteps.

The behavior of the coupled THM system at $t = t_f$, as obtained by a direct FE simulation, is described in Figure 2. The pore pressure distribution is maximal closer to the glacier front's initial location as expected. The vertical displacement of the rock mass is negative under the glacier (compression) but exhibits positive values outside the glacier, indicating heaving which is typically observed with glacial loading [50]. The non-uniform temperature distribution under the glacier indicates that steady-state condition is not yet reached after 6000 years.

5.1.2 Dual Problem

For the setup of the dual problem, we consider the QoI as the average pressure in the domain Ω combined with the average vertical displacement in the upper surface Γ_{TOP} over time $t = (0, t_f]$,

$$\begin{aligned} \hat{J}(T,\mathbf{u},p) = &\frac{1}{|\Gamma_{\text{TOP}}|} \int_0^{t_f} \int_{\Gamma_T} \mathbf{u}\; d\Gamma_T\; dt \\ &+ \hat{\alpha} \frac{1}{|\Omega|} \int_0^{t_f} \int_{\Omega} p\; d\Omega\; dt. \end{aligned} \tag{41}$$

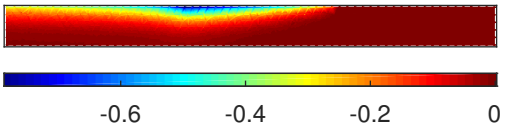

(a) FE Temperature, T (°C)

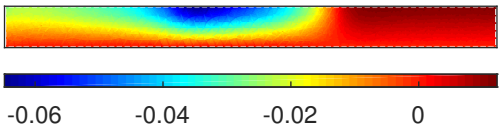

(b) FE z-Displacement, u_z (m)

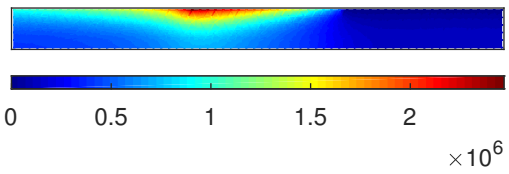

(c) FE Pore Pressure, p (Pa)

Fig. 2 Evolution of thermo-hydro-mechanical fields after 6000 years

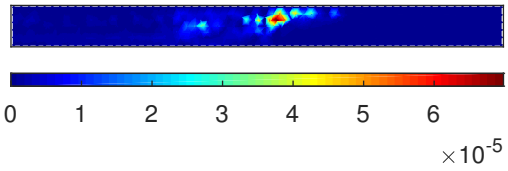

(a) $\frac{|T-T_N|}{\|T\|_{\max}}$

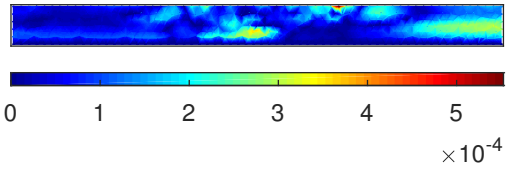

(b) $\frac{|u_z-u_{zN}|}{\|u_z\|_{\max}}$

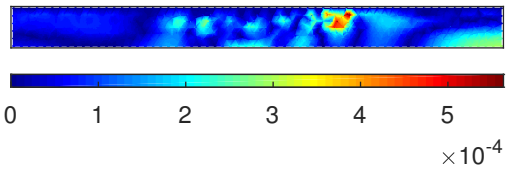

(c) $\frac{|p-p_N|}{\|p\|_{\max}}$

Fig. 3 Error map of FE and RB-projected coupled THM solution. Error is expressed relative to the maximum field value of the FE solution.

Applying the formulation for the backward-in-time evolving dual problem (32-35), we obtain the adjoint solution corresponding to the temperature, displacement and pressure fields. The dual problem is solved with the same spatial and time discretization as the primal problem. Figure 4 shows the backward propagation of the adjoint for the vertical displacement in the upper surface with zero initial condition imposed at the final time.

The adjoint solution is verified by showing that the QoI estimated by relating the source term and adjoint (21) holds. Figure 5 shows the accuracy of the source term-adjoint estimate with respect to the spatial and time discretization refinement. It is observed that the time discretization of the dual problem affects the QoI estimate convergence more dominantly than the spatial discretization refinement in this particular case where the QoI is chosen as a functional of field solutions in the entire time span $t : (0, t_f]$.

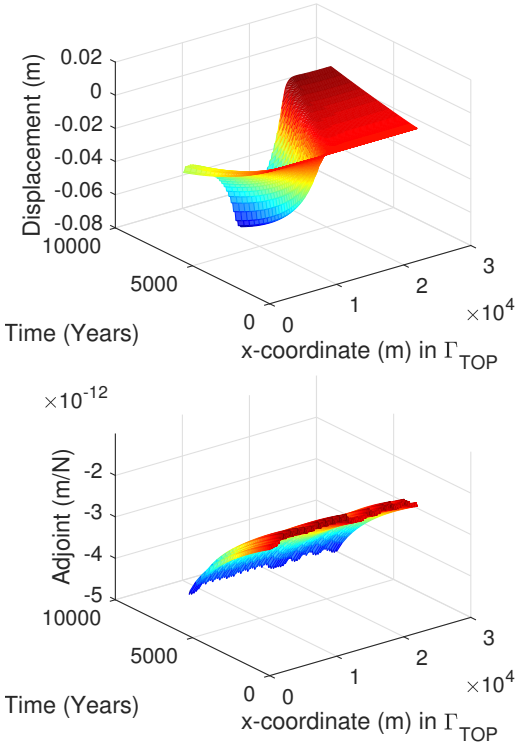

Fig. 4 Vertical displacement of the primal problem (top) and the corresponding adjoint solution (bottom) in the upper surface of the domain Γ_{TOP}

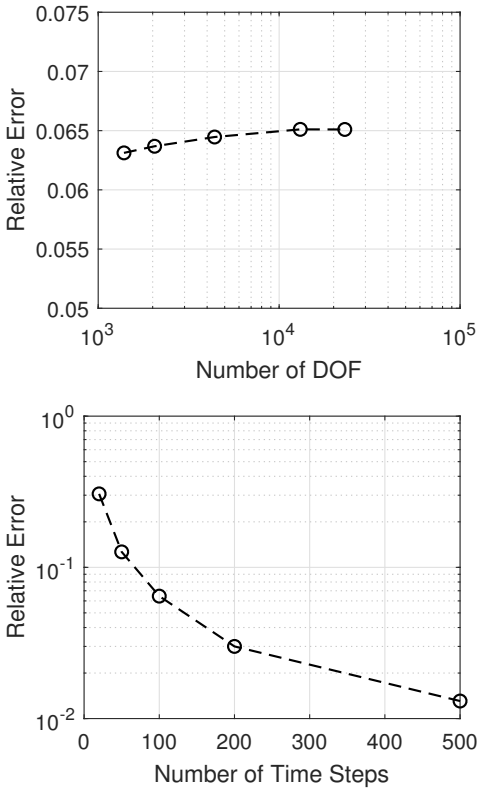

Fig. 5 Error plot verifying $J(T, u, p) = L(T_{adj}, u_{adj}, p_{adj})$ with respect to mesh refinement (top) and time step refinement (bottom)

5.1.3 Reduced Basis Generation

This 2D coupled THM problem is parametrized by varying some of the parameters related to material properties. The elastic modulus and permeability corresponding to the mechanical and hydraulic properties are selected to vary within a range of realistic values for a granitic type of rock; elastic modulus $\mu_1 : [1.5 \times 10^{10},\ 4.4{\times}10^{10}]$ Pa and permeability $\mu_2 : [1{\times}10^{-24},\ 1{\times}10^{-18}]$ m^2. The parametric training sample is discretized with 1050 parameter sets ($n_{\mu_1} \times n_{\mu_2} = 35 \times 30$), where each set contains the 2 material properties $\boldsymbol{\mu}_n = (\mu_1, \mu_2)$.

The formulation of the error in the QoI at a certain parameter set is equivalent to the product of the residual and the adjoint solution evaluated in that parameter set. Recalling that the computational cost involved in the solution of the dual problem is the same as in the primal problem, if the adjoint solution is evaluated for each parameter set in the training sample, $(T_{adj}(\boldsymbol{\mu}_n), u_{adj}(\boldsymbol{\mu}_n), p_{adj}(\boldsymbol{\mu}_n))$, it is equivalent to solving the full order (FE) model 1050 times at each enrichment step.

$$\begin{aligned}\hat{J}(e_T(\boldsymbol{\mu}), e_{\mathbf{u}}(\boldsymbol{\mu}), e_p(\boldsymbol{\mu})) :&= \hat{R}(T_{adj}(\boldsymbol{\mu}), \mathbf{u}_{adj}(\boldsymbol{\mu}), p_{adj}(\boldsymbol{\mu})) \\ &= \Delta(\boldsymbol{\mu})\end{aligned} \tag{42}$$

To avoid this extremely expensive procedure, we impose a condition based on the assumption that the adjoint solution is not very sensitive with respect to parametric variations. We therefore solve the dual problem only once in a selected parameter set ($\boldsymbol{\mu}^0$); and this adjoint solution is assumed to be sufficient to be reused for evaluating the error estimate in the entire training sample. The enrichment procedure is stopped once the normalized estimated error in QoI is below the prescribed tolerance level of 10^{-4}.

In the present case, the greedy adaptive procedure required 9 enrichment steps to reach the error level below 10^{-4}. The corresponding number of POD modes at a truncation tolerance of 10^{-5} on their relative amplitude after each enrichment step is shown in Figure 6.

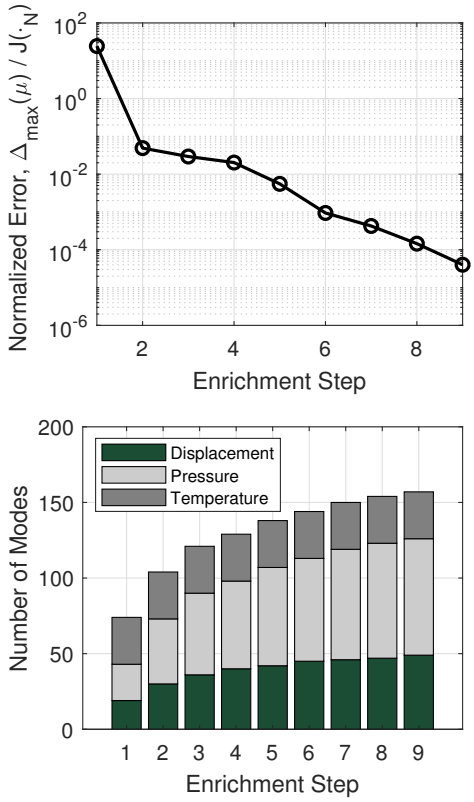

Fig. 6 Convergence of greedy-based strategy to the prescribed tolerance level, $\frac{\Delta_{max}(\mu)}{\hat{J}(\cdot_N)}$ (top) and number of POD modes at each enrichment step (bottom)

The accuracy of the projected RB solution with respect to the FE model is qualitatively assessed in Figure 3. The evolution of the temperature, displacement and pore pressure fields after 6000 years is accurately depicted as shown in the error map distribution of the THM fields in the domain. The accuracy is quantitatively assessed in the entire parametric training sample by looking at the global error norm in the domain in Table 3. The error norm is computed at every parameter set in the training sample and plotted in Figure 7. With a maximum error on the order of 10^{-7} for temperature, and 10^{-3} for displacement and pore pressure, the projected RB solution is in good agreement with the reference FE solution.

Table 3 Maximum error level in the entire parametric training sample

$\max\left[\frac{e_T(\boldsymbol{\mu})}{T(\boldsymbol{\mu})}\right]$	$\max\left[\frac{e_{\mathbf{u}}(\boldsymbol{\mu})}{\mathbf{u}(\boldsymbol{\mu})}\right]$	$\max\left[\frac{e_p(\boldsymbol{\mu})}{p(\boldsymbol{\mu})}\right]$
1.8×10^{-7}	1.1×10^{-3}	7.8×10^{-3}

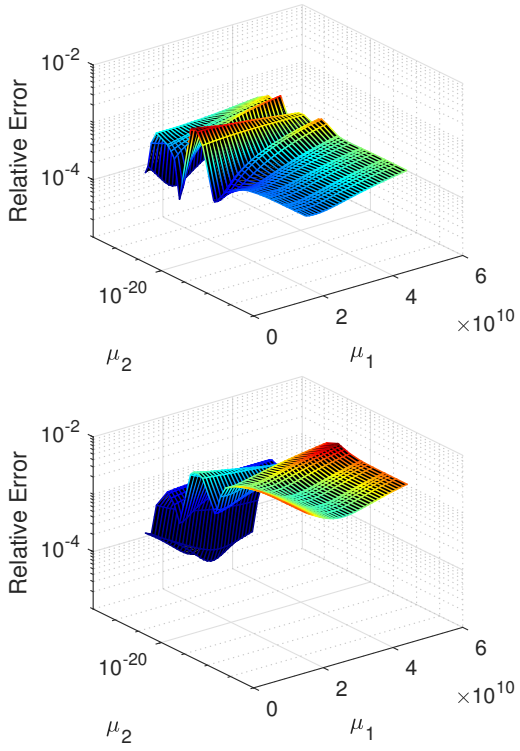

Fig. 7 Error in the entire parametric training sample: displacement $\| \frac{e_{\mathbf{u}}}{\mathbf{u}} \|$ (top) and pressure $\| \frac{e_p}{p} \|$ (bottom)

5.1.4 Efficiency of the Goal Oriented Error Estimator

To assess the efficiency of the goal-oriented error estimator, the effectivity index describing the rigor and sharpness of the estimate is measured. The effectivity index is computed as

$$\eta(\boldsymbol{\mu}) = \frac{J(e(\boldsymbol{\mu}))}{\Delta(\boldsymbol{\mu})} \tag{43}$$

where $\Delta(\boldsymbol{\mu})$ is the estimated error and $J(e(\boldsymbol{\mu}))$ is the exact error evaluated in the QoI. Ideally, it is desired to have $\eta \equiv 1$ to obtain a sharp bound for the error.

By first evaluating the effectivity index in the parameter, $\boldsymbol{\mu}^0$, where the adjoint is computed (Figure 8), it is shown that the error estimator indeed yields a sharp bound with an index value of 1.05 for the given spatial and time discretization (Table 4).

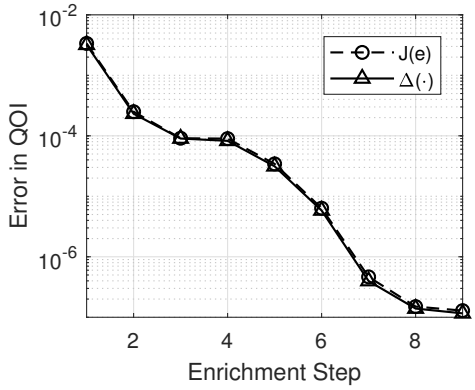

Fig. 8 Efficiency of goal-oriented error estimator with respect to basis enrichment - assessed at parameter set where the adjoint is evaluated ($\boldsymbol{\mu}^0$)

Table 4 Effectivity index of error estimator within the parameteric training sample

Point	$J(e(\boldsymbol{\mu}))$	$\Delta(\boldsymbol{\mu})$	$\eta(\boldsymbol{\mu})$
$\boldsymbol{\mu}^0$	3.4×10^{-3}	3.2×10^{-3}	1.05
$\boldsymbol{\mu}^a$	1.37×10^{-2}	1.17×10^{-1}	0.12
$\boldsymbol{\mu}^b$	1.35×10^{-2}	1.16×10^{-1}	0.12
$\boldsymbol{\mu}^c$	1.34×10^{-2}	1.15×10^{-1}	0.12
$\boldsymbol{\mu}^d$	3.2×10^{-3}	3.7×10^{-3}	0.87
$\boldsymbol{\mu}^e$	3.4×10^{-3}	3.0×10^{-3}	1.13
$\boldsymbol{\mu}^f$	6.44×10^{-5}	1.68×10^{-5}	3.83
$\boldsymbol{\mu}^g$	2.48×10^{-6}	3.28×10^{-6}	0.75
$\boldsymbol{\mu}^h$	1.75×10^{-5}	2.08×10^{-5}	0.84

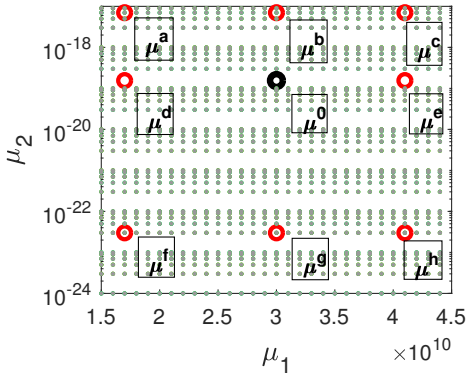

Fig. 9 Selected parameters where effectivity index is evaluated

To investigate the effect of solving the adjoint only in one parameter set and reusing it for the entire training sample, the sensitivity of the adjoint is evaluated by computing the effectivity indices at different points in the training sample (Figure 9). The corresponding effectivity indices at these points are reported in Table 4. The error estimator performs well with the maximum underestimation index less than 5 ($\eta(\boldsymbol{\mu}^f) = 3.83$) for the parameter sets tested. As expected, the effectivity index gets worse when the parameter set is further from the reference adjoint parameter $\boldsymbol{\mu}^0$. There is no conclusive observation when an overestimation or an underestimation occurs (i.e. the error is overestimated in both cases where the permeability is lower ($\boldsymbol{\mu}^g$) and higher ($\boldsymbol{\mu}^b$) than the adjoint's permeability).

5.2 3D Advancing Glacier Problem

To illustrate more quantitatively the computational gain that can be expected from the proposed methodology, the 2D homogeneous rock mass subjected to an advancing glacier model is now extended to a more realistic 3D problem.

The geometry of the 3D homogeneous rock mass (Figure 10) is taken from the topography of a valley located in southern Andes. For the FE model, 27-node hexahedral elements are used to interpolate the solution with quadratic shape functions for displacement and linear shape functions for pore pressure and temperature fields to ensure the stability of the coupled system. The 3D domain is a 22000m by 10200m region with non-uniform thickness characterizing the valley with a maximum elevation of +1341m and a minimum elevation of -3985m. The discretized domain consists of 3774 hexahedral elements, 34125 nodes and 115833 DOF. The time discretization is kept the same as in the 2D case with 100 time steps for an observation period of 6000 years.

The QoI is taken as the average of the pressure in the whole domain and the average of the vertical displacement along the upper surface. The glacier advance on the upper surface is described by the same function as in the 2D problem (37), imposed at zero-elevation. The elevation profile of the glacier is extruded along the lateral direction and enforced to conform to the rock

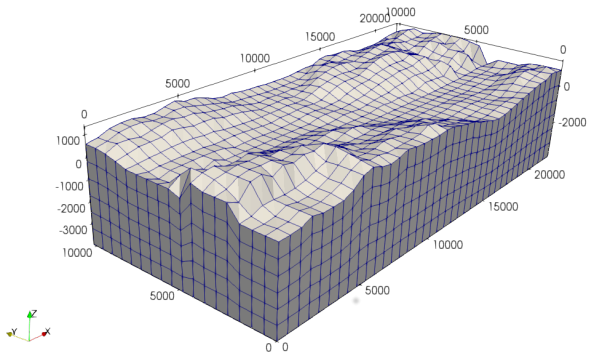

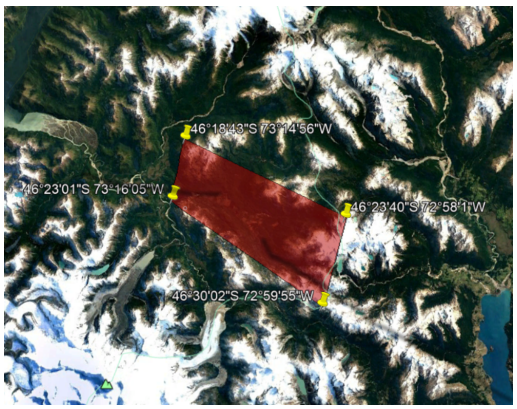

Fig. 10 Homegeneous rock mass valley with non-uniform top elevation taken from a region in southern Andes

mass elevation (i.e., when the effective glacier thickness is lower than the rock mass elevation at a specific point, no loading is applied).

To build the reduced basis, the coupled system is parametrized as in the 2D case. The ranges of values for the elastic modulus μ_1 and the permeability μ_2 are varied and discretized to 70 sets ($n_{\mu_1} \times n_{\mu_2} = 10 \times 7$), defining the parametric training sample. Implementing the greedy adaptive strategy, it took 8 enrichment steps to reach the tolerance level below 10^{-4}. The reduced basis after enrichment contains 306 POD modes in total, resulting in RB spaces with characteristic size of 48, 79 and 179 modes for temperature, displacement and pore pressure, respectively.

The dimensionality of the coupled THM system is thus significantly reduced – having only 306 DOF instead of 115833 DOF to solve the primal problem. Comparing the computational costs, the FE model solution with 115833 DOF requires 17683 seconds (4.6 hours) in MATLAB implementation while the RB-projected system takes 35 seconds to run which yields a computational gain of 505x speed up, see Table 5. Note that with even more realistic (i.e. larger) problems and involving more parameters, the expected speed up is even higher.

Table 5 Computational gain with RB model in 3D application

	FE Model	RB Model	Gain
DOF	115 833	306	**378:1**
CPU Time	17 683s	35s	**505x***speed up*

The accuracy of the RB-projected solution is assessed by comparing it to the FE model solution evaluated for a reference parameter set value presented in [48] (3×10^{10} Pa, 1.55×10^{-19} m^2), which is not used as a snapshot point to build the RB. Figure 11 and Figure 12 show that the temperature, displacement and pore pressure field distributions in the domain after 6000 years are recovered well by the RB model. The relative error norms in the QoI at 6000 years are 4.3×10^{-4} for pore pressure and 2.6×10^{-5} for displacement which gives a good level of accuracy for the RB approximation. Further comparison of RB-projected solutions to FE model solutions (Table 6) is performed for different parameter set values chosen by varying parameter μ_1 or μ_2 with respect to the reference parameter set which is useful for sensitivity analysis of the parametric system.

Table 6 Relative error in the pore pressure and displacement fields evaluated in the QoI domain (temperature field is unaffected by μ_1 and μ_2)

μ_1(Pa)	μ_2(m^2)	$\frac{\|e_p^*\|}{\|p^*\|}$	$\frac{\|e_{\mathbf{u}}^*\|}{\|\mathbf{u}^*\|}$
3.0×10^{10}	1.55×10^{-19}	4.3×10^{-4}	2.6×10^{-5}
3.0×10^{10}	6.00×10^{-18}	9.3×10^{-3}	4.4×10^{-4}
2.4×10^{10}	1.55×10^{-19}	3.3×10^{-4}	1.6×10^{-5}
3.5×10^{10}	1.55×10^{-19}	4.1×10^{-4}	2.5×10^{-5}
3.0×10^{10}	1.00×10^{-21}	3.8×10^{-4}	1.5×10^{-5}

* evaluated in the QoI, at time=6000 years

6 Conclusion

We presented a strategy to solve transient coupled THM systems in the framework of reduced basis approximation. To preserve the stability properties of the reference FE model, the same interpolation principle is applied in the RB projection by using three separate bases - each basis corresponding respectively to temperature,

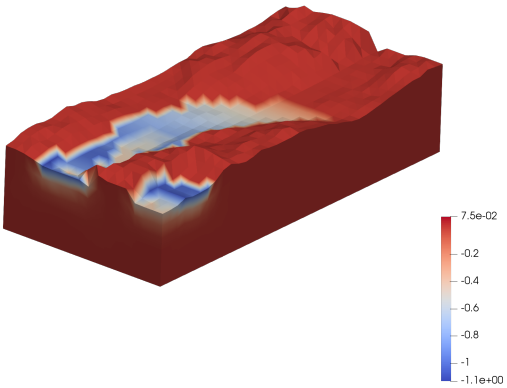

(a) FE Temperature, T (°C)

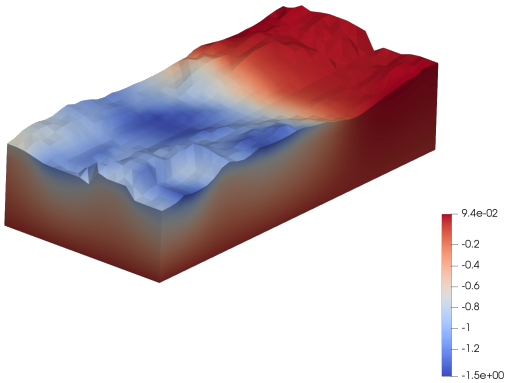

(b) FE z-Displacement, u_z (m)

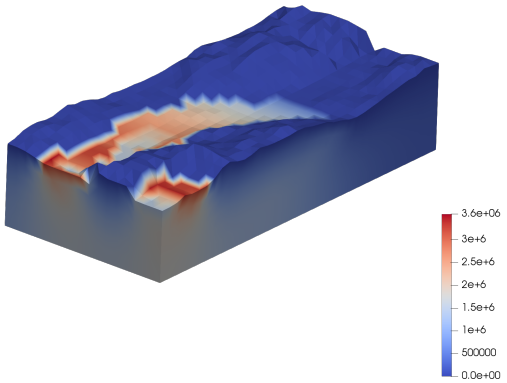

(c) FE Pore Pressure, p (Pa)

Fig. 11 3D Evolution of thermo-hydro-mechanical properties after 6000 years

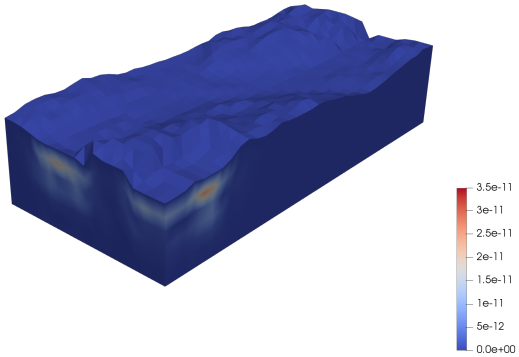

(a) $\frac{|T-T_N|}{\|T\|_{\max}}$

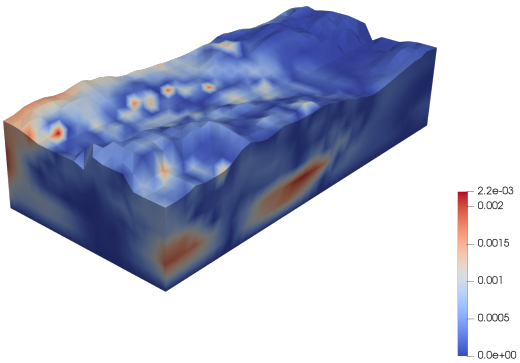

(b) $\frac{|u_z-u_{zN}|}{\|u_z\|_{\max}}$

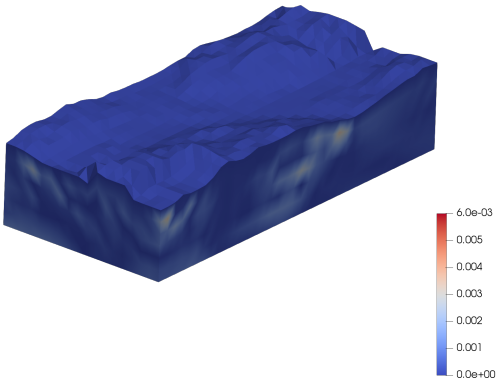

(c) $\frac{|p-p_N|}{\|p\|_{\max}}$

Fig. 12 Error map of FE and RB-projected coupled THM solution. Error is expressed relative to the maximum field value of the FE solution.

displacement and pore pressure fields. The greedy adaptive strategy, employed to optimally enrich the bases, strongly relies on the error estimator that provides the criterion to select the next snapshots and certifies the RB-projected solutions.

We developed an efficient a-posteriori error estimator for the coupled THM system which evaluates the error in specific quantities of interest. The strength of this goal-oriented scheme lies in the combination of implicit and explicit error assessment approaches - first, assessing the error implicitly in the dual problem and then injecting it to the explicitly evaluated primal residual. Particularly for a time-dependent system, this error assessment enables a simplified implementation that adapts the space-time grid such that at every time step, the adjoint is simply plugged in to the weak residual. For computational efficiency, it was proven for the application examples that solving the adjoint only once and reusing it for error evaluation in the entire training sample is effective as evident in the sharp error estimates.

The numerical examples demonstrated the ability of the RB strategy to accurately approximate the reference FE solutions of the coupled THM system with a significant reduction in computational costs. Furthermore, higher computational gain is foreseen for more complex and realistic problems that feature non-linearity, heterogeneity and higher-dimensional parametric space. For problems that deal with much larger sets of uncertain parameters, it is worth investigating in future works whether the scheme of solving the dual problem only at one parameter set can provide sufficiently sharp error estimates. Potential strategies (e.g., interpolation and iterative optimization procedures) that tackle such issue are to be explored.

Acknowledgements We acknowledge the funding support from the European Commission Education, Audiovisual and Culture Executive Agency (EACEA) under Erasmus Mundus Joint Doctorate Simulation in Engineering and Entrepreneurship Development (SEED), FPA 2013-0043. S. Zlotnik would like to thank the funding from the Generalitat de Catalunya 2017-SGR-1278, the project DPI2017-85139-C2-2-R funded by the Spanish Ministry and the project H2020-RISE MATHROCKS GA n° 777778. T.J. Massart acknowledges the support of FRS-FNRS through grant 26033553 EnLightenIt. We would also like to thank SCK-CEN for the valuable interactions related to coupled systems in nuclear waste repository applications.

References

1. Baldi G, Hueckel T, Peano A, Pellegrini R (1991) Developments in modelling of thermo-hydro-geomechanical behaviour of Boom clay and clay-based buffer materials (Volume 2) Final report, Report EUR-13365/2. Commission of the European Community
2. Horseman ST, Winter MG, Entwistle DC (1987) Geotechnical Characterization of Boom Clay in Relation to the Disposal of Radioactive Waste. Commission of the European Community
3. Sultan N, Delage P, Cui YJ (2002) Temperature effects on the volume change behaviour of Boom clay. Engineering Geology 64 (2–3), 135–145
4. Sultan, N, Cui YJ, Delage P (2010) Yielding and plastic behaviour of Boom Clay. Géotechnique 60 (9), 657–666
5. Deng YF, Tang AM, Cui YJ, Nguyen XP, Li XL, Wouters L (2011) Laboratory Hydromechanical Characterisation of Boom Clay at Essen and Mol. Physics and Chemistry of the Earth, Parts A,B,C, Clays in Natural and Engineered Barriers for Radioactive Waste Confinement 36 (17–18), 1878–1890
6. Deng YF, Tang AM, Cui YJ, Li XL (2011) Study on the hydraulic conductivity of Boom clay. Canadian Geotechnical Journal 48 (10), 1461–1470
7. Deng YF, Cui YJ, Tang AM, Li XL, Sillen X (2012) An experimental study on the secondary deformation of Boom clay. Applied Clay Science 59–60, 19–25
8. Olivella S, Gens A (2005) Double structure THM analyses of a heating test in a fractured tuff incorporating intrinsic permeability variations. International Journal of Rock Mechanics and Mining Sciences, 42 (5-6), 667-679
9. Onofrei C, Gray M (1996) Modelling hygro-thermo-mechanical behaviour of engineered clay barriers: validation phase. Engineering Geology 41 (1), 301-318
10. Chandler NA, Wan AWL, Raoch PJ (1998) The buffer/container experiment design and construction report. AECL-11792, COG-97-186-I, AECL
11. Chijimatsu M, Fujita T, Sugita Y, Amemiya K, Kobayashi A (2001) Field experiment, results and THM behavior in the Kamaishi mine experiment. International Journal of Rock Mechanics and Mining Science, 38(1): 67-78
12. Collin F, Li XL, Radu JP, Charlier R (2002) Thermo-hydro-mechanical coupling in clay barriers. Engineering Geology 64 (2–3), 179–193
13. ENRESSA (2010) FEBEX project: Full-scale engineered barriers experiment for a deep geological repository for high-level radioactive waste in crystalline host rock, Final report. ENRESSA
14. Thomas HR, He Y, (1998) Modelling the behaviour of unsaturated soil using an elastoplastic constitutive relationship", Géotechnique, 48(5), 589-603
15. Francois B, Laloui L, Laurent C (2009) Thermo-hydro-mechanical simulation of ATLAS in situ large scale test in Boom Clay. Computers and Geotechnics 36 (4), 626–640
16. Jha B, Juanes R (2014) Coupled Multiphase Flow and Poromechanics: A Computational Model of Pore Pressure Effects on Fault Slip and Earthquake Triggering. Water Res. Res., 50(5), 3776–3808
17. Nowak T, Kunz H, Dixon D, Wang W, Görke U, Kolditz O (2011) Coupled 3D THM analysis of geotechnical in-situ tests, Int. J. of Rock Mech. Min. Sci., 48(1), 1-15
18. Aagaard BT, Knepley MG, Williams CA (2013) A domain decomposition approach to implementing fault slip in finite-element models of quasi-static and dynamic crustal deformation, J. Geophys. Res. Solid Earth, 118, 3059–3079
19. Martini I, Rozza G, Haasdonk B (2015) Reduced basis approximation and a-posteriori error estimation for the coupled stokes-darcy system. Advances in Computational Mathematics 41(5):1131–1157

20. Carey JW, Harp D, Lewis K, Chu S, Kelkar S (2017) A Reduced-Order Model for Wellbore Permeability Induced by Geomechanical Damage; NRAP-TRS-III-006-2017; NRAP Technical Report Series; U.S. Department of Energy, National Energy Technology Laboratory: Morgantown, WV
21. Florez H (2017) Applications of Model-Order Reduction to Thermo-Poroelasticity. American Rock Mechanics Association
22. Huerta A, Diez P (2016) Implicit residual type error estimators, A: Verifying Calculations: forty years on, Springer, p. 19-32
23. Zhang Y, Feng L, Li, S, Benner P (2015) An efficient output error estimation for model order reduction of parametrized evolution equations. SIAM Journal on Scientific Computing. 37. B910-B936. 10.1137/140998603
24. Grepl MA (2012) Certified reduced basis methods for nonaffine linear time-varying and nonlinear parabolic partial differential equations. Math. Models Methods Appl. Sci., 22
25. Grepl MA, Patera AT (2005) A posteriori error bounds for reduced-basis approximations of parametrized parabolic partial differential equations. M2AN Math. Model. Numer. Anal., 39 , pp. 157–181
26. Haasdonk B, Ohlberger M (2008) Reduced basis method for finite volume approximations of parametrized linear evolution equations. M2AN Math. Model. Numer. Anal., 42, pp. 277–302
27. Nguyen NC, Rozza G, Patera AT (2009) Reduced basis approximation and a posteriori error estimation for the time-dependent viscous Burgers' equation, Calcolo, 46, pp. 157–185
28. Prudhomme C, Rovas DV, Veroy K, Machiels L, Maday Y, Patera AT, Turinici G (2002) Reliable real-time solution of parametrized partial differential equations: Reduced-basis output bound methods, J. Fluids Engrg., 124, pp. 70–80
29. Fuentes D, Littlefield D, Oden JT, Prudhomme S (2006) Extensions of goal-oriented error estimation methods to simulations of highly-nonlinear response of shock-loaded elastomer-reinforced structures, Comput Methods Appl Mech Engrg 195, 4659–4680
30. Díez P, Calderon G (2007) Goal-oriented error estimation for transient parabolic problems, Comput Mech 39, 631–646
31. Parés N, Díez P, Huerta A (2008) Bounds of functional outputs for parabolic problems. Part I: exact bounds of the discontinuous galerkin time discretization, Comput Methods Appl Mech Eng 197:1641–1660
32. Parés N, Díez P, Huerta A (2008) Bounds of functional outputs for parabolic problems. Part II: bounds of the exact solution. Comput Methods Appl Mech Eng 197:1661–1679
33. Schmich M, Vexler B (2008) Adaptivity with dynamic meshes for space–time finite element discretization of parabolic equations. SIAM J Sci Comput 30, 369–393
34. Verdugo F, Parés N, Díez P (2014) Goal-oriented space-time adaptivity for transient dynamics using a modal description of the adjoint solution, Comput Mech 54: 331
35. Bermejo R, Carpio J (2009) A space–time adaptive finite element algorithm based on dual weighted residual methodology for parabolic equations. SIAM J Sci Comput 31, 3324-3355
36. Zee KG, Oden JT, Prudhomme S, Hawkins-Daarud A (2010) Goal-oriented error estimation for Cahn-Hilliard models of binary phase transition. Numerical Methods for Partial Differential Equations, 27(1), 160-196
37. Nguyen T, Selvadurai A., Coupled thermal-mechanical-hydrological behaviour of sparsely fractured rock: implications for nuclear fuel waste disposal. International Journal of Rock Mechanics and Mining Sciences and Geomechanics Abstracts 32(5): 465–479 (1995)
38. Babuška I (1973) The finite element method with Lagrangian multipliers. Numerische Mathematik, 20(3):179–192
39. Brezzi F, Douglas J, Marini LD (1985) Two families of mixed finite elements for second order elliptic problems. Numerische Mathematik, 47:217–235
40. Bathe KJ (2001) The inf-sup condition and its evaluation for mixed finite element methods. Computers and Structures 79(2):243–252
41. Zienkiewicz OC, Chan A, Pastor M, Schrefler B, Shiomi T (1999) Computational Geomechanics with Special Reference to Earthquake Engineering. Wiley: Chichester, UK
42. Lewis RB, Schrefler BA (1998) The Finite Element Method in the Static and Dynamic Deformation and Consolidation of Porous Media (Second Edition). Wiley
43. Patera AT, Rozza G (2007) Reduced Basis Approximation and a Posteriori Error Estimation for Parametrized Partial Differential Equations, MIT, Cambridge, MA
44. Amsallem D, Farhat C (2012) Stabilization of projection-based reduced-order models. Internat. J. Numer. Methods Engrg., 91, pp. 358–377
45. Reis T, Stykel T (2007) Stability analysis and model order reduction of coupled systems. Math. Comput. Model. Dyn. Syst., 13, pp. 413–436
46. Rozza G, Veroy K (2007) On the stability of the reduced basis method for Stokes equations in parametrized domains, Comput. Methods Appl. Mech. Engrg., 196, pp. 1244–1260
47. Kalashnikova I,Bloemen Waanders Bv, Arunajatesan S, Barone M (2014) Stabilization of projection-based reduced order models for linear time-invariant systems via optimization-based eigenvalue reassignment. Computer Methods in Applied Mechanics and Engineering, Volume 272, Pages 251-270, ISSN 0045-7825
48. Selvadurai APS, Suvorov AP, Selvadurai PA (2015) Thermo-hydro-mechanical processes in fractured rock formations during a glacial advance. Geosci. Model Dev., 8, 2167-2185